The Astrophysical Journal, 991:214 (11pp), 2025 October 1 https://doi.org/10.3847/1538-4357/adfed0

Radial Evolution of Turbulence Spectra on the Jovian Magnetosheath Flanks: Juno Observations

Hui Li[1,2], Haoyu Li[1,2], Zhongwei Yang[1,2], and Chi Wang[1,2]
[1] State Key Laboratory of Solar Activity and Space Weather, National Space Science Center, Chinese Academy of Sciences, Beijing, 100190, People's Republic of China; hli@nssc.ac.cn
[2] University of Chinese Academy of Sciences, Beijing, People's Republic of China
Received 2025 January 9; revised 2025 August 5; accepted 2025 August 19; published 2025 September 30

Abstract

The Jovian magnetosheath provides a unique environment for examining the radial evolution of magnetosheath turbulence due to its large spatial extent. Utilizing magnetic field measurements from the Juno spacecraft, this study examines the radial evolution of magnetic field turbulence on the flanks of the Jovian magnetosheath. We find that turbulence on the dawn flank evolves significantly after crossing the bow shock. In contrast, the dusk flank exhibits a flattening of the power spectrum at MHD scales, attributed to the presence of mirror modes. Wave analysis based on the singular value decomposition method confirms the role of mirror modes in causing spectral flattening. Statistical results reinforce the connection between mirror modes and spectral flattening and reveal a dawn–dusk asymmetry in the distribution of mirror modes.

Unified Astronomy Thesaurus concepts: Planetary magnetospheres (997); Interplanetary turbulence (830)

1. Introduction

The Jovian magnetosheath is not only a critical interface for the exchange of energy and mass between the solar wind and the Jovian magnetosphere but also a dynamic environment where plasma instabilities and turbulence are prevalent. The study of turbulence in the magnetosheath is essential for understanding the multiscale and nonlinear interactions that govern energy dissipation, particle heating, and acceleration processes (S. D. Bale et al. 2005; R. Bandyopadhyay et al. 2018).

Turbulence analysis in the solar wind and magnetosheath has been facilitated by examining the power spectral density (PSD), which reveals the scaling laws of magnetic field fluctuations across four distinguishable dynamic scales (e.g., O. Alexandrova et al. 2008; F. Sahraoui et al. 2009; G. Zimbardo et al. 2010; R. Chhiber et al. 2018; W. M. Macek et al. 2018; H. Li et al. 2020, and others). The inertial range, or MHD-scale range relevant to this study, is characterized by a power-law scaling of $f^{-5/3}$ (A. Kolmogorov 1941) or $f^{-3/2}$ (P. S. Iroshnikov 1964; R. H. Kraichnan 1965) for the magnetic field fluctuations, which has been observed in the solar wind (S. D. Bale et al. 2005; R. Bandyopadhyay et al. 2018; C. H. K. Chen et al. 2020; O. W. Roberts et al. 2023, and others) and across various planetary magnetosheaths such as Earth (O. Alexandrova et al. 2008; S. Y. Huang et al. 2017; H. Li et al. 2020), Mars (W. Jiang et al. 2023; H. Li et al. 2024), Mercury (S. Y. Huang et al. 2020), Venus (S. Xiao et al. 2020), Jupiter (R. Bandyopadhyay et al. 2021; N. Andrés et al. 2023), and Saturn (L. Z. Hadid et al. 2015).

Postshock turbulence evolution in the magnetosheath is a complex process, with the cascade of energy extending to larger scales and the turbulence eventually restoring to its preshock state (S. Y. Huang et al. 2017; H. Li et al. 2020). If the turbulence correlation length L_c (the maximum scale in the inertial range) is much larger than the ion characteristic scale L_i in the magnetosheath (such as the proton inertial length d_i or proton gyroradius ρ_i), it can be assumed that the turbulence cascade transitions from the L_c scale to the L_i scale, allowing for the observation of the inertial range. Previous studies on turbulence evolution in Earth's magnetosheath have provided several insights. S. Y. Huang et al. (2017) found that the PSDs of magnetic field fluctuations at MHD scales typically exhibit an f^{-1} scaling (similar to the energy-containing scale in solar wind turbulence), while $f^{-5/3}$ scaling is observed only in specific events on the flanks and magnetopause regions. H. Li et al. (2020) reported that along the radial direction, the spectral index of the inertial range gradually decreases from the bow shock to the magnetopause and is positively correlated with the Alfvén Mach number M_A, with this spatial evolution being independent of upstream solar wind conditions. However, the developed turbulence observed in Earth's magnetosheath could also be locally generated by instabilities such as Kelvin–Helmholtz waves at the magnetopause (e.g., H. Hasegawa et al. 2004). Selecting a planetary magnetosheath that allows for more extensive turbulence development is necessary to eliminate such effects.

Due to its large spatial extent, the Jovian magnetosheath provides a unique environment for examining the radial evolution of magnetosheath turbulence. For example, the correlation length L_c of turbulence in the Jovian magnetosheath can reach up to $3200di$ (R. Bandyopadhyay et al. 2021). In comparison, the L_c in Earth's magnetosheath is about $10di$ near the subsolar region, approximately $200di$ on the flanks, and typically around $40di$ (J. E. Stawarz et al. 2022). Thus, the Jovian magnetosheath turbulence has sufficient time to develop. Additionally, Jupiter's large-scale magnetosheath experiences longer magnetosheath-crossing events, which are beneficial for a more detailed study of turbulence evolution in different regions of the magnetosheath.

F. L. Scarf et al. (1979) were the first to observe plasma turbulence fluctuations within the Jovian magnetosheath using Voyager 1, and subsequent studies have utilized data from Voyager and Ulysses (R. R. Anderson 1983; M. J. A. Bolzan

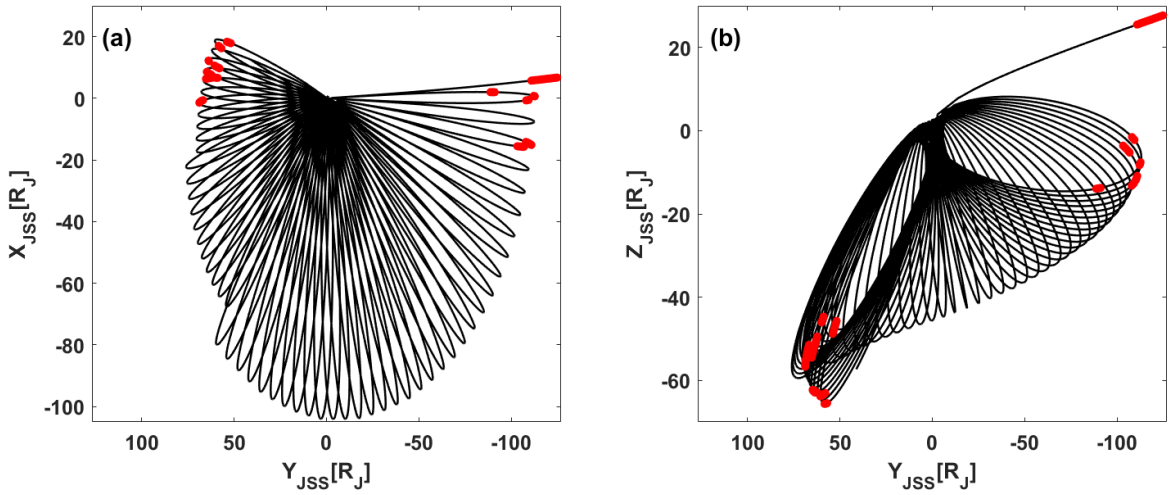

Figure 1. Juno's trajectory in the JSS coordinate system (*X*-axis points toward the Sun, *Z*-axis is along the Jupiter north pole) in (a) *X*–*Y* plane and (b) *Y*–*Z* plane. Red dots indicate the positions of events analyzed in this work.

& E. Echer 2014). In recent years, R. Bandyopadhyay et al. (2021) and N. Andrés et al. (2023) have analyzed plasma turbulence and turbulence energy cascade rates using the Juno Magnetometer (MAG) and ion (JADE) instruments on the Juno spacecraft. However, previous studies have not focused on the evolution of turbulence in the Jovian magnetosheath and the effects of plasma fluctuations and structures on turbulence.

Magnetosheath contains a variety of fluctuations and instabilities, such as mirror modes, ion cyclotron waves, and the Kelvin–Helmholtz instability. These fluctuations and instabilities can influence turbulence, thereby altering the local power spectrum characteristics (e.g., E. A. Lucek et al. 1999; Y. Matsumoto & M. Hoshino 2004; F. Sahraoui et al. 2006; M. W. Kunz et al. 2014; J. E. Stawarz et al. 2016; H. Li et al. 2024). At the same time, the energy injection caused by waves and instabilities generated by pickup ions also influences the properties of the turbulence in both the magnetosheath (W. Jiang et al. 2023; H. Li et al. 2024) and heliosheath (L.-L. Zhao et al. 2024). Therefore, when analyzing the changes in the turbulence power spectrum, it is essential to consider the localized wave characteristics.

In this study, we employ magnetic field measurements from the Juno spacecraft to investigate the spectral evolution of turbulence on the flanks of the Jovian magnetosheath and analyze the impact of local fluctuations on turbulence. Our analysis focuses on the radial variation of the power spectral index and the effect of mirror modes on the magnetic field turbulence, revealing a dawn–dusk asymmetry in the distribution of these modes. This investigation contributes to the broader understanding of plasma dynamics in the Jovian magnetosheath and provides insights into the role of mirror modes in modulating turbulence characteristics. Section 2 describes the data set and methodology used in this study. Section 3 presents the case studies and statistical results on the evolution of the turbulence spectrum, the magnetic compressibility, and wave analysis using the singular value decomposition (SVD) method. Section 4 discusses our results and their implications. Finally, Section 5 summarizes our findings.

2. Data Set and Methodology

The analysis presented in this study is based on data collected by the Juno spacecraft, which was launched on 2011 August 5, and entered the Jovian magnetosheath for the first time on 2016 June 24 (J. E. P. Connerney et al. 2017a; D. J. McComas et al. 2017). Juno's orbit, with the orbital period of 53 days and the apojove at 113 Jupiter radii (S. J. Bolton et al. 2017), allows it to traverse the Jovian magnetosheath multiple times during its mission. Currently, Juno is operating on the dusk flank of Jupiter, enabling the comparison of the Jovian magnetosheath turbulence on both the dawn and dusk flanks. Figure 1 shows Juno's trajectory in the Jupiter-De-Spun-Sun (JSS) coordinate system.

2.1. MAG and WAVE Instrument

This study utilizes data from the MAG and WAVE instruments onboard Juno, which are crucial for examining the magnetic field and plasma wave characteristics within the magnetosheath. The MAG investigation consists of two vector fluxgate magnetometers that measure the magnetic field (J. E. P. Connerney et al. 2017b). For this study, the magnetic field data were standardized to a time resolution of 8 Hz to ensure consistency across the data set. The Juno Waves (WAVE) investigation measures plasma waves in the electric and magnetic fields (W. S. Kurth et al. 2017). This study uses the electric field data collected by the low-frequency receiver, which has a time resolution of 1 s and a frequency range of 50–20 kHz.

2.2. Event Selection

For the dawn flank, we relied on the event list provided by G. B. Hospodarsky et al. (2017), selecting eight complete magnetosheath crossing events. For the dusk flank, bow shock (BS) and magnetopause (MP) crossings from 2021 to 2023 were determined using the method outlined by G. B. Hospodarsky et al. (2017), identifying BS crossings by increases in the magnetic field strength and changes in the electric field, and MP crossings by increases in the magnetic field strength and the appearance or disappearance of trapped continuum radiation in the electric field. All 18 events are

Table 1
List of the Jovian Magnetosheath Crossing Events Made by Juno from 2016 to 2023

Event	Start Time	End Time	Type	Frequency Range/Hz	θ_{BN}
dawn1	2016-06-24T08:16	2016-06-25T21:20	in	0.002–0.015	$70.^{\circ}2$
dawn2	2016-07-16T23:07	2016-07-17T15:33	out	0.002–0.03	$64.^{\circ}0$
dawn3	2016-07-28T21:02	2016-07-30T00:22	in	0.002–0.025	$70.^{\circ}8$
dawn4	2016-08-07T01:20	2016-08-08T01:39	out	0.001–0.02	$59.^{\circ}3$
dawn5	2016-11-09T18:09	2016-11-11T02:36	out	0.001–0.02	$60.^{\circ}7$
dawn6	2016-11-11T23:21	2016-11-13T19:55	in	0.002–0.025	$57.^{\circ}9$
dawn7	2016-11-21T22:39	2016-11-23T16:49	out	0.002–0.03	$69.^{\circ}7$
dawn8	2016-11-23T16:54	2016-11-24T04:01	in	0.002–0.03	$80.^{\circ}6$
dusk1	2023-03-22T23:06	2023-03-24T10:26	out	0.001–0.015	$84.^{\circ}1$
dusk2	2023-03-24T19:20	2023-03-26T10:16	in	0.002–0.015	$77.^{\circ}6$
dusk3	2023-06-09T19:29	2023-06-12T06:14	out	0.002–0.03	$76.^{\circ}6$
dusk4	2023-06-13T14:24	2023-06-14T02:27	in	0.002–0.015	$85.^{\circ}3$
dusk5	2023-07-09T05:36	2023-07-11T17:23	out	0.002–0.015	$78.^{\circ}8$
dusk6	2023-07-11T19:21	2023-07-12T05:45	in	0.002–0.02	$58.^{\circ}2$
dusk7	2023-08-14T07:01	2023-08-16T03:57	in	0.002–0.015	$73.^{\circ}2$
dusk8	2023-08-19T21:37	2023-08-20T14:29	in	0.002–0.02	$63.^{\circ}5$
dusk9	2023-10-30T22:22	2023-11-01T07:04	in	0.002–0.015	$69.^{\circ}4$
dusk10	2023-11-13T02:23	2023-11-14T02:37	in	0.002–0.02	$70.^{\circ}3$

Note. The type means that Juno crossed the magnetosheath from the solar wind to the magnetosphere (in) or from the magnetosphere to the solar wind (out). The frequency range of the MHD scales calculated for each event is also given. The angle (θ_{BN}) between the upstream interplanetary magnetic field and the normal direction of the shock surface is computed from the MVA technique.

listed in Table 1. To investigate the turbulence characteristics in different regions of the magnetosheath, we selected events with durations greater than 10 hr. This criterion allows us to divide each event into multiple segments for analysis. Using the minimum variance analysis (MVA) method, we calculate the angle (θ_{BN}) between the upstream interplanetary magnetic field and the normal direction of the shock surface. The average θ_{BN} on the dawn flank is $64.^{\circ}7 \pm 5.^{\circ}5$, and the average θ_{BN} on the dusk flank is $73.^{\circ}7 \pm 8.^{\circ}6$. There are no cases of quasi-parallel shock in our events.

The PSDs of the magnetic field were calculated using Welch's method. The frequency range used for calculating the slopes at MHD scales for each event is given in Table 1. The SVD method was employed for wave analysis, allowing us to derive parameters such as ellipticity and wave normal angle from the magnetic field data alone (O. Santolík et al. 2003). This technique enables the identification of waves within the magnetosheath. We quantified the magnetic field compressibility using the parameter $C_{\parallel}$ (ratio between the PSDs of the parallel to total magnetic field fluctuation), which is used in S. Y. Huang et al. (2017): $C_{\parallel}(f) = |\delta B_{\parallel}(f)|^2/(|\delta B_{\parallel}(f)|^2 + |\delta B_{\perp}(f)|^2)$. We calculated the average $C_{\parallel}$ using the frequency range in Table 1.

3. Result

3.1. Case Studies

Figures 2 and 3 present two examples of the Jovian magnetosheath crossing events observed on the dawn and dusk flanks, respectively. The power spectral index at MHD scales is calculated within the frequency range of 0.002–0.015 Hz using least squares fitting. For the SVD method, the background magnetic field was determined by applying a low-pass filter with a cutoff frequency of 10^{-4} Hz. We calculated the magnetic field compressibility $C_{\parallel}$ and the average $C_{\parallel}$ within the frequency range, which is the same as that used for calculating the power spectral index.

3.1.1. Dawn Flank

Figure 2 shows observations of a magnetosheath crossing event on the dawn flank. Magnetic field data are presented in Figures 2(a) and (b). Juno entered the magnetosheath from the solar wind (BS crossing) at 08:16 UTC on 2016 June 24, and exited the magnetosheath (MP crossing) at 21:20 UTC on 2016 June 25. Changes in the magnetic field are observed near the BS and MP regions, which are consistent with previous descriptions. The wave normal angle and ellipticity calculated from the SVD method are shown in Figures 2(c) and (d). Fluctuations in the magnetosheath may affect turbulence and modify the power spectrum at MHD scales, leading to broadband spectral behavior. Based on the wave normal angle and ellipticity, different waves, such as ion cyclotron waves (e.g., W. Jiang et al. 2023; H. Li et al. 2024) and mirror modes (e.g., G. Erdős & A. Balogh 1996; M. Volwerk et al. 2016; A. P. Dimmock et al. 2022; S. W. Cyril et al. 2023), can be identified.

The ion cyclotron waves are left-hand polarized (ellipticity close to -1) and quasi-parallel propagating (wave normal angle close to 0). Mirror modes are linearly polarized (ellipticity $= 0$) and usually quasi-perpendicular propagating (wave normal angle close to 90°). The main type of magnetic field fluctuations at the MHD scales that we are discussing is the magnetic mirror modes. At the same time, we also observe the presence of ion cyclotron waves. Due to the higher frequency of these fluctuations (about 10^{-1} Hz, outside of the considered range of scales), no further analysis was conducted in this article. We exclusively consider fluctuations for which the wave normal angle $>75^{\circ}$ and the absolute value of ellipticity <0.15. This allows for a clearer demonstration of regions with highly oblique propagation and near-linear polarization. The 2D maps of ellipticity and wave normal angle, before any masking, are provided in Appendix A.

Figures 2(e)–(g) show the magnetic field spectra and spectral indices in the shaded regions in Figures 2(a)–(b) of the magnetosheath. The spectrum follows a power law of the form $\sim f^{-1.58}$ near the bow shock region, $\sim f^{-1.67}$ in the middle

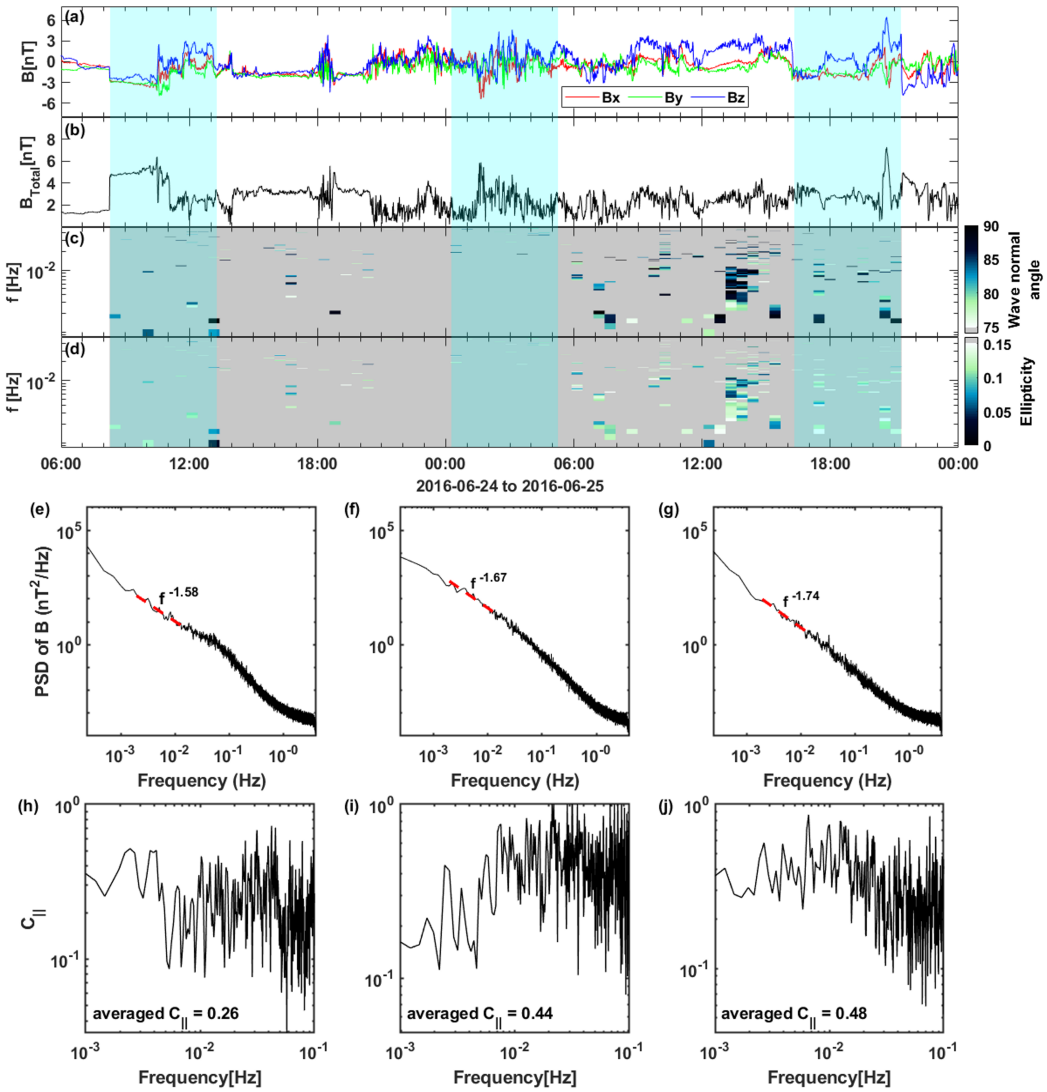

Figure 2. An example of the Jovian magnetosheath crossing event observed on the dawn flank. (a) The components of the magnetic field. (b) Total magnetic field. (c) Wave normal angle. (d) Absolute value of ellipticity. (e)–(g) PSDs of the magnetic field for three shaded time intervals, and the frequency range for calculating the power spectral index is 0.002–0.015 Hz. (h)–(j) The magnetic compressibility $C_{\parallel}$ for three shaded time intervals.

magnetosheath region, and $\sim f^{-1.74}$ near the magnetopause region. From the bow shock to the magnetopause, the power spectral index of the magnetic field gradually decreases, which is consistent with results from studies of Earth's magnetosheath (H. Li et al. 2020). Figures 2(h)–(j) show the magnetic compressibility $C_{\parallel}$ in the three shaded regions. We calculated the averaged $C_{\parallel}$ for the corresponding frequency bands, and the results were 0.26, 0.44, and 0.48, respectively.

3.1.2. Dusk Flank

Figure 3 presents observations of a magnetosheath crossing event on the dusk flank. Juno entered the magnetosheath from the magnetosphere (MP crossing) at 05:36 UTC on 2023 July 9, and exited the magnetosheath (BS crossing) at 17:23 UTC on 2023 July 11. Similar changes in the magnetic field are observed near the BS and MP regions. The wave normal angle and ellipticity are shown in Figures 3(c) and (d). For this event, quasiperiodic changes (primarily decreases) in the magnetic field are observed in several regions within the magnetosheath. The corresponding wave characteristics exhibit quasi-perpendicular propagation (wave normal angle close to 90°) and linear polarization (ellipticity close to 0). At the same time, we find that the compressibility of the magnetic field in this region is also significantly higher than that in other regions without highly oblique and linearly polarized characteristics (see Appendix A). The hodograms of the magnetic field fluctuations computed from the MVA technique (see Appendix B) also indicate the presence of nearly linearly polarized waves. These characteristics are consistent with the features of mirror modes. Mirror modes are ubiquitous in the space plasma environment, typically observed in high β plasmas, and are compressive structures not propagating in the ion rest frame. Based on the magnetic field observations, the mirror modes are characterized by significant disturbances in the magnetic field strength, with the direction of maximum variance aligned with the magnetic field direction (S. P. Joy et al. 2006; A. P. Dimmock et al. 2022). The presence of mirror modes has previously been observed in Jupiter's magnetosheath (S. P. Joy et al. 2006).

Figures 3(e)–(g) show the magnetic field spectra and spectral indices in different regions (the shaded regions in

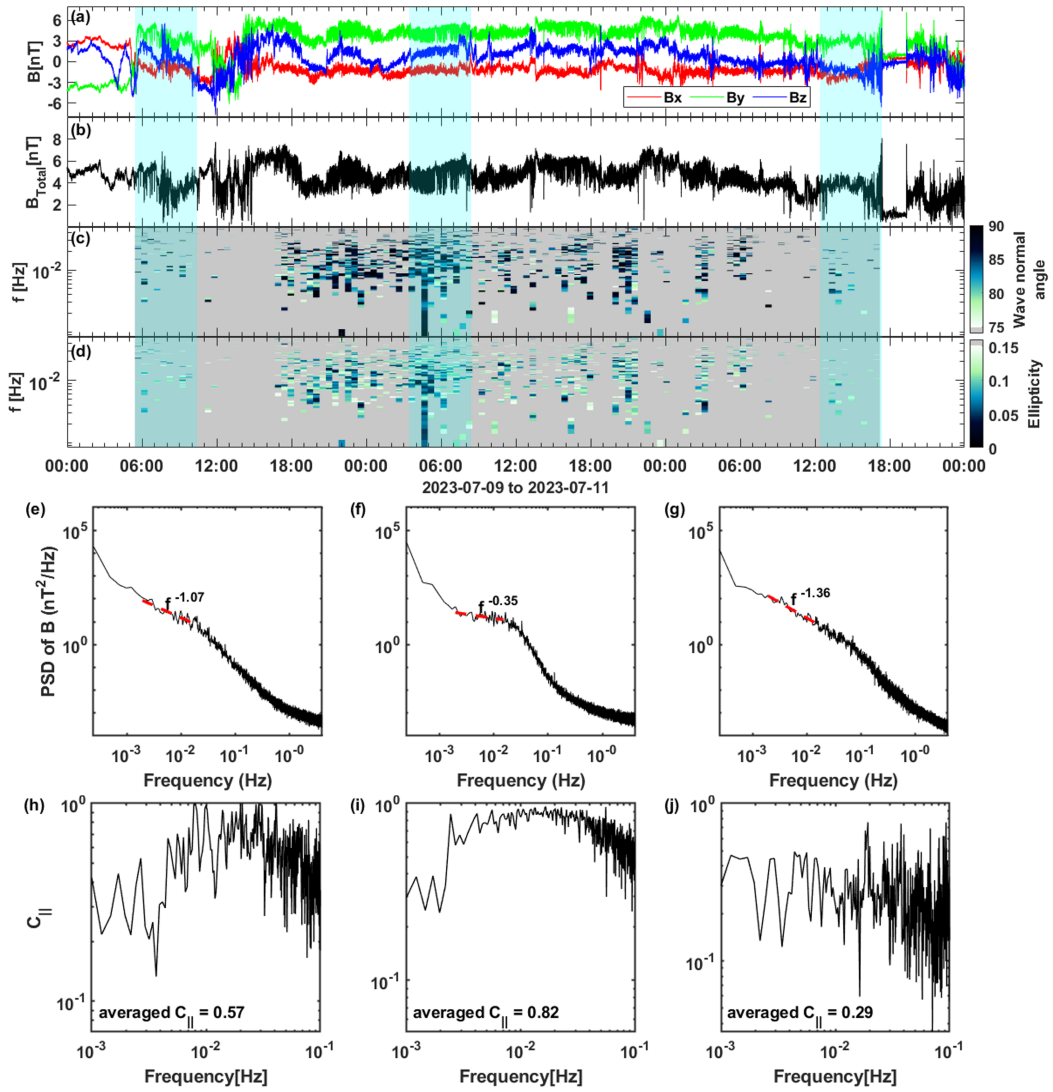

Figure 3. An example of the Jovian magnetosheath crossing event observed on the dusk flank. (a) The components of the magnetic field. (b) Total magnetic field. (c) Wave normal angle. (d) Absolute value of ellipticity. (e)–(g) PSDs of the magnetic field for three shaded time intervals, and the frequency range for calculating the power spectral index is 0.002–0.015 Hz. (h)–(j) The magnetic compressibility $C_{\parallel}$ for three shaded time intervals.

Figures 3(a)–(d)) of the magnetosheath. The spectrum follows a power law of the form $\sim f^{-1.36}$ near the bow shock region, $\sim f^{-0.35}$ in the middle magnetosheath region, and $\sim f^{-1.07}$ near the magnetopause region. Compared to the dawn flank, mirror modes are more frequently observed on the dusk flank. Thus, the spectral index in the middle magnetosheath is larger than that near the BS and the MP regions. Figures 3(h)–(j) show the magnetic compressibility $C_{\parallel}$ of the three shaded regions. The averaged $C_{\parallel}$ values are 0.57, 0.82, and 0.29, respectively. The results reveal high compressibility near the bow shock and in the middle magnetosheath. The results indicate the presence of high compressibility, highly oblique propagation, and nearly linearly polarized magnetic field fluctuations in these regions. We believe these fluctuations are mirror modes or "mirror-mode-like structures."

3.2. Statistical Results

Case studies reveal different radial variations of the spectral index in the Jovian magnetosheath. On the dawn flank, the spectral index gradually decreases from the bow shock to the magnetopause, whereas on the dusk flank, it increases within the middle magnetosheath. To investigate these differences, we calculated spectral indices and averaged $C_{\parallel}$ at MHD scales for each event from the bow shock using a 5 hr window and normalized them based on their fractional time distance: $D_{\rm frac} = \frac{T_{\rm Juno} - T_{\rm BS}}{T_{\rm MP} - T_{\rm BS}} \times 100\%$, where $T_{\rm BS}$ and $T_{\rm MP}$ represent the time of the BS and MP crossing, and $T_{\rm Juno}$ represents the time away from the BS crossing. We divided each event into three regions: BS vicinity ($D_{\rm frac}$ from 0% to 20%), the middle magnetosheath ($D_{\rm frac}$ from 20% to 80%), and MP vicinity ($D_{\rm frac}$ from 80% to 100%). Figure 4 presents the radial evolution of the turbulence spectral indices, magnetic field compressibility, ellipticity, and wave normal angle in the magnetosheath.

Figure 4(a) shows the turbulence spectral indices in different regions of the Jovian magnetosheath, with red representing the dawn flank and blue representing the dusk flank. The vertical lines represent the standard deviation. On the dawn flank, the turbulence spectral index gradually decreases from approximately $f^{-1.4}$ to $f^{-5/3}$ after crossing

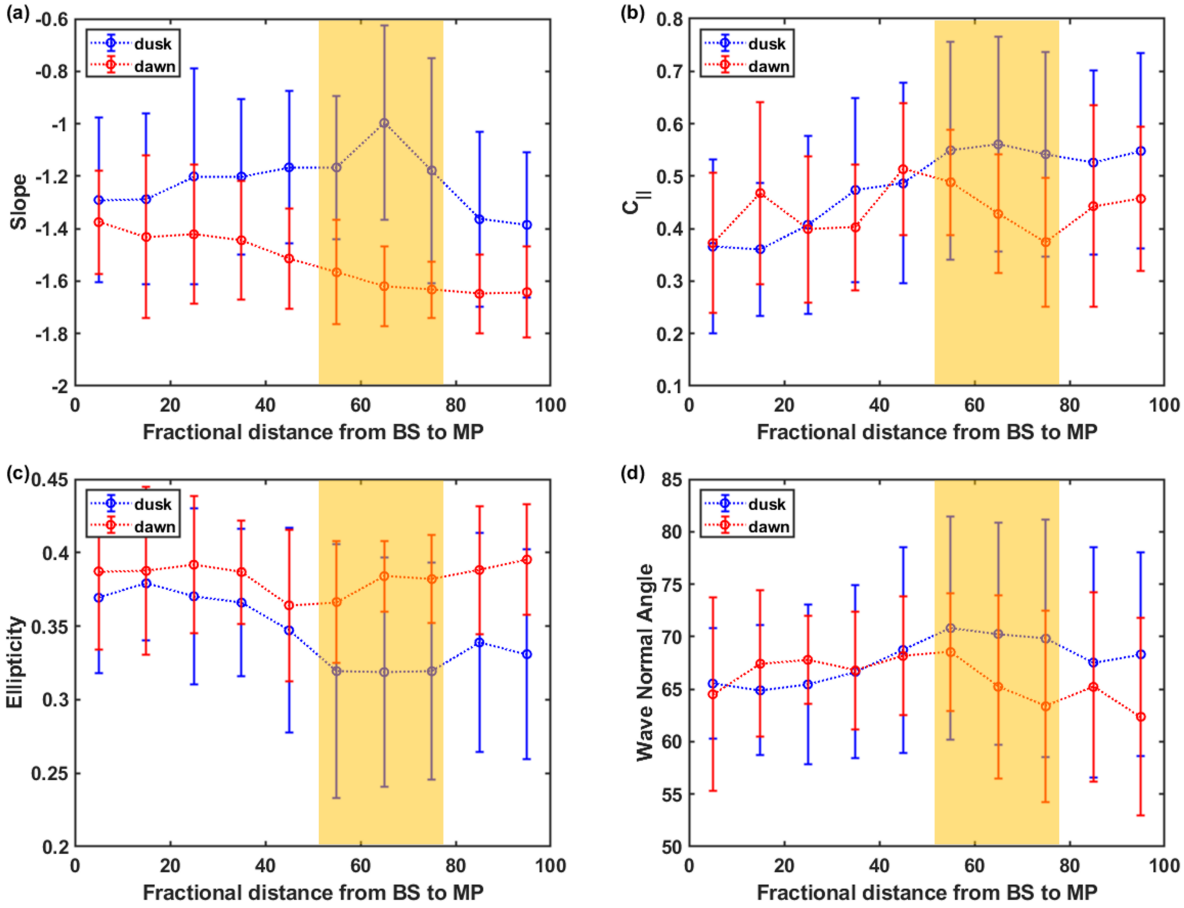

Figure 4. Radial evolution of (a) spectral index, (b) averaged magnetic compressibility $C_{||}$, (c) ellipticity, and (d) wave normal angle, with the dawn flank in red and the dusk flank in blue. The highlighted region marks the central magnetosheath region where the spectral index difference is most pronounced.

the bow shock. This evolutionary trend is similar to observations at Earth (e.g., S. Y. Huang et al. 2017; H. Li et al. 2020). It is generally believed that the solar wind turbulence evolves after crossing the bow shock, causing the gradual decrease of the spectral index. However, unlike observations in Earth's magnetosheath ($\sim f^{-1.54}$ obtained by H. Li et al. 2020), we observe the $\sim f^{-5/3}$ scaling in the middle magnetosheath, indicating that the turbulence has already undergone substantial evolution within the magnetosheath, consistent with our previous estimations.

On the dusk flank, the turbulence spectral index increases from $\sim f^{-1.3}$ to $\sim f^{-1}$ after crossing the BS and then gradually decreases to $\sim f^{-1.4}$ closer to the MP. This differs from observations in Earth's magnetosheath and the Jovian dawn-flank magnetosheath, revealing a dawn–dusk asymmetry in the turbulence evolution on the flanks of the Jovian magnetosheath. In the region where $D_{\rm frac}$ from 50% to 70% (highlighted in yellow), the spectral index shows the most significant difference between the dawn flank and dusk flank. The statistical results are consistent with the radial variation of spectral indices reported in the case studies (Section 3.1).

Figures 4(b)–(d) show the averaged magnetic compressibility $C_{||}$, ellipticity, and wave normal angle in different regions of the Jovian magnetosheath, with red representing the dawn flank and blue representing the dusk flank. There is also a marked dawn–dusk difference in the middle magnetosheath (MSH) ($D_{\rm frac}$ from 50% to 70%, highlighted in yellow), in agreement with the spectral index. In this region, the spectral index on the dusk flank is significantly higher than that on the dawn flank, indicating the flattening of the power spectrum. The dusk flank has smaller ellipticity (near-linear polarization), a larger wave normal angle (highly oblique propagation), and higher compressibility. These characteristics are consistent with those of the mirror modes.

Based on the case analyses (Figures 2 and 3) and statistical analyses (Figure 4), we suggest that the difference might be attributed to mirror modes in the Jovian magnetosheath. As observed, the magnetic field power spectrum is flatter in regions with a higher prevalence of mirror modes. This relationship will be verified through statistical analysis.

To further investigate the impact of the mirror modes on turbulence, we averaged the absolute value of ellipticity and $C_{||}$ for each event within the frequency range given in Table 1 using a 5 hr window. When averaging, we only calculated the ellipticity of fluctuations with the wave normal angle above 75°, so that the results can better represent the proportion of mirror modes in different regions. We calculated the results for different regions of the magnetosheath and normalized them based on the fractional distance, $D_{\rm frac}$. Figure 5 shows the distribution of ellipticity versus the spectral indices and averaged $C_{||}$ values. To exclude the effects of boundary layers (like Kelvin-Helmholtz instability near MP), we separate the data into the BS vicinity and the MP vicinity.

Figures 5(a) and (b) show the results of ellipticity for the interior and boundary regions of the magnetosheath, respectively, with black representing the dawn flank and red

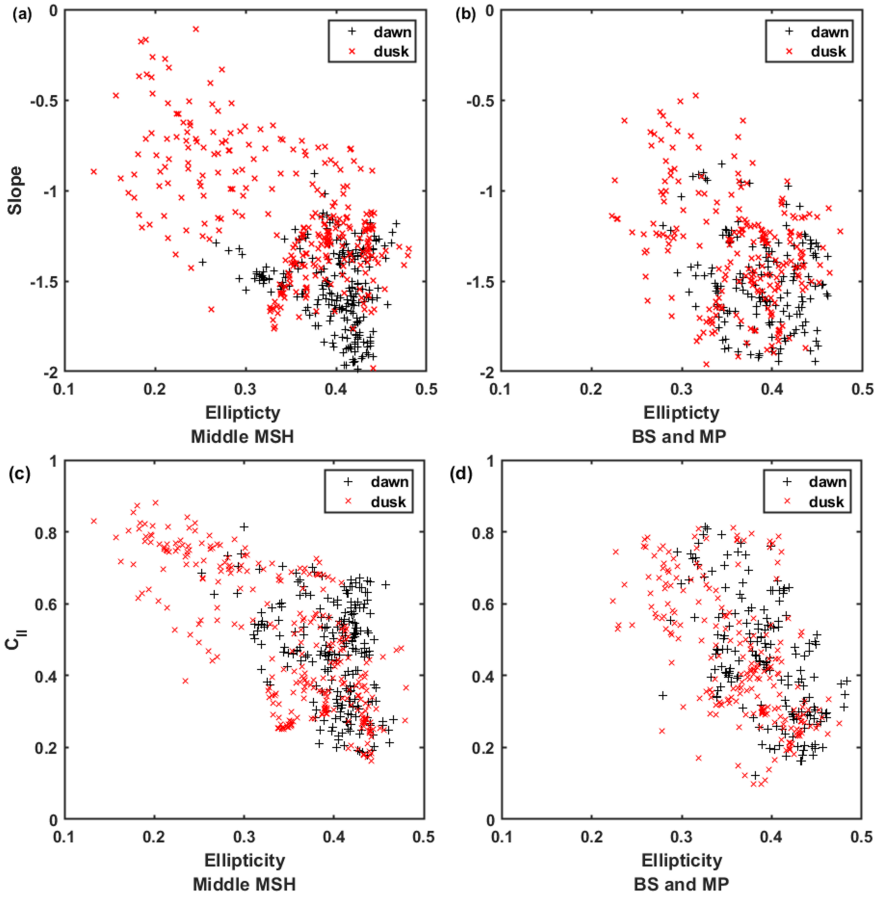

Figure 5. The distribution of ellipticity vs. the spectral indices in (a) and (b) and averaged $C_{||}$ values in (c) and (d).

representing the dusk flank. Consistent with the case study results, it is observed in the magnetosheath that as ellipticity approaches 0, indicating a significant presence of the mirror modes in that region, the spectral indices gradually increase, demonstrating a correlation between them. Similar results were observed in the boundary region, although they are less pronounced. These findings suggest that the presence of mirror modes leads to an increase in the magnetic field turbulence spectral indices (i.e., the flattening of the power spectrum). Figures 5(c) and (d) show the results of averaged $C_{||}$ for the interior and boundary regions of the magnetosheath, respectively, with black representing the dawn flank and red representing the dusk flank. Consistent with the trends shown in Figures 5(a) and (b), we observe an inverse relationship between the ellipticity and magnetic compressibility. There are more regions with high compressibility and linear polarization on the dusk flank, indicating a higher occurrence of mirror modes. This suggests that the distribution of mirror modes is uneven between the dawn and dusk flanks.

4. Discussion

Mirror modes, a common plasma phenomenon, have been observed in Jupiter's magnetosheath (e.g., S. P. Joy et al. 2006). S. P. Joy et al. (2006) have provided the spatial distribution of mirror modes within Jupiter's magnetosheath, but no significant dawn–dusk asymmetry, as shown in Figure 5, has been observed. We quantified the occurrence rates of mirror modes across both flanks. A time period is classified as containing mirror modes if there is at least one result within the frequency range (consistent with the frequency range in Table 1) that simultaneously satisfies the conditions of wave normal angle $>75°$ and the absolute value of ellipticity <0.15. We refer to the ratio of the periods in which mirror modes exist to all periods of time as the occurrence of mirror modes. The dusk flank (53%) exhibits a higher occurrence of mirror modes than the dawn flank (39%).

The dusk-flank events selected in this study are located closer to Jupiter compared to the dawn-flank events (the average distance of the dawn-flank bow shock is 109.31 R_j, while the average distance of the dusk-flank bow shock is 85.08 R_j). Therefore, on the dusk flank, the compressive effect of the solar wind on the magnetosheath is more pronounced, leading to more intense ion heating (P. Wu et al. 2009). Additionally, the average value of θ_{BN} of these events on the dawn flank is $64.^{\circ}7 \pm 5.^{\circ}5$, and that on the dusk flank is $73.^{\circ}7 \pm 8.^{\circ}6$. Bow shocks in our selected events are predominantly quasi-perpendicular, and ions are mainly heated in the perpendicular direction (C. F. Kennel et al. 1985; B. T. Tsurutani et al. 2011). This enhances the temperature anisotropy, which favors the generation of mirror modes (S. P. Joy et al. 2006; M. Volwerk et al. 2008). The reasons for the dawn–dusk asymmetry of mirror modes warrant further investigation through additional observations or numerical simulations.

We also conducted a statistical analysis of events with $\theta_{BN} < 65°$ and $\theta_{BN} > 75°$ to discuss the differences under different θ_{BN} conditions. Figure 6 presents the probability

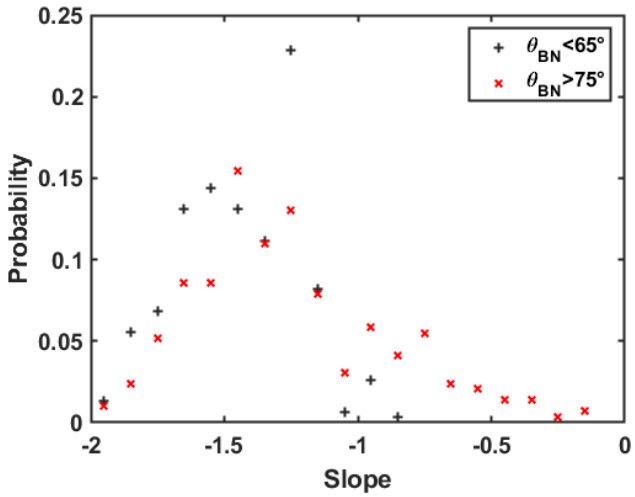

Figure 6. The probability distribution of the corresponding spectral indices for events with $\theta_{BN} < 65°$ and $\theta_{BN} > 75°$.

distribution of the corresponding spectral indices for these events, respectively, with black representing events where $\theta_{BN} < 65°$ and red representing events where $\theta_{BN} > 75°$. The spectral indices of events with $\theta_{BN} < 65°$ are mainly distributed between $\sim f^{-1}$ and $\sim f^{-2}$, while those of events with $\theta_{BN} > 75°$ are more widely distributed but still predominantly fall between $\sim f^{-1}$ and $\sim f^{-2}$. We did not find significant differences in the turbulence properties between these two groups of events. At present, we are unable to categorize the events by bow shock types based on the current data set and will conduct further analysis on this issue in future Juno observations.

In general, the generation conditions for mirror modes and ion cyclotron waves are similar (S. P. Joy et al. 2006; J. Soucek et al. 2015). However, in this study, we primarily observe mirror modes, with ion cyclotron waves detected only in rare cases and at higher frequencies. In plasma environments, ion cyclotron waves typically dissipate more rapidly (due to higher damping) and are suppressed by mirror modes under high plasma β conditions (M. Shoji et al. 2009; J. Soucek et al. 2015). The large-scale magnetosheath of Jupiter causes the solar wind to take a longer time to travel from the subsolar point to the flanks, and the plasma β within the magnetosheath is relatively high (with an average value of 4.79, according to D. A. Ranquist et al. 2019). Therefore, it is reasonable to primarily observe the presence of mirror modes.

Previous studies have analyzed the impact of mirror modes on turbulence (e.g., F. Sahraoui et al. 2006). However, these studies primarily focused on smaller scales, and the effect of large-scale mirror modes ($\sim 10^2$ s) observed in the Jovian magnetosheath on turbulence remains poorly understood. Due to the lack of plasma data, this study could not address the effect of mirror modes on turbulence dissipation in the Jovian magnetosheath. Further investigation of this topic will be necessary in future research.

5. Summary

In this study, we analyzed the turbulence characteristics and wave features of 18 Jovian magnetosheath crossing events observed by Juno from 2016 to 2023 using power spectral analysis and the singular value decomposition (SVD) method. Our findings can be summarized as follows:

1. Turbulence evolution on the dawn flank: The turbulence in the dawn magnetosheath undergoes significant evolution after crossing the bow shock, similar to that observed in the Earth's magnetosheath. This evolution is characterized by a gradual decrease in the power spectral index from the bow shock to the magnetopause, indicating turbulence evolution within the magnetosheath.
2. Turbulence evolution on the dusk flank: In contrast, the turbulence in the dusk-flank magnetosheath exhibits a unique behavior, with the power spectral index initially increasing within the magnetosheath before decreasing toward the magnetopause. This suggests a more complex interaction between the turbulence and the local plasma environment on the dusk flank.
3. Dawn–dusk asymmetry and role of mirror modes: Wave analysis using the SVD method and magnetic compressibility revealed the presence of continuous mirror modes in the Jovian magnetosheath. The distribution of mirror modes exhibits a dusk-enhanced dawn–dusk asymmetry. Mirror modes are associated with the flattening of the PSDs of the magnetic field turbulence, particularly in regions where mirror modes are more prevalent. This finding highlights the significant impact of mirror modes on the turbulence characteristics within the Jovian magnetosheath.

Acknowledgments

We thank the entire Juno team for providing the data. MAG and WAVE data are publicly available through the Planetary Data System. The Juno Waves data (JNO-E/J/SS-WAV-3-CDR-SRVFULL-V2.0) are available from the PDS at doi:10.17189/1520498 (W. S. Kurth & C. W. Piker 2024). The Juno MAG data (JNO-J-3-FGM-CAL-V1.0) are also available from the PDS at doi:10.17189/1519711 (J. E. P. Connerney 2024). Juno ephemeris (Figure 1 in JSS coordinate) are retrieved from https://wgc.jpl.nasa.gov:8443/webgeocalc/#StateVector. SVD method for wave analysis was performed using the IRFU-Matlab analysis package (Y. Khotyaintsev et al. 2024) available at https://github.com/irfu/irfu-matlab. This work is supported by NNSFC grants (42374198, 42188101, 42150105, and 42274210), the project of Civil Aerospace "14th Five Year Plan" Preliminary Research in Space Science (D010202 and D010301). H.L. is also supported by the China-Brazil Joint Laboratory for Space Weather (No. 119GJHZ2024027MI). Z.Y. is also supported by the National Key R&D Program of China (No. 2021YFA0718600), the Specialized Research Fund for State Key Laboratories of China.

Appendix A
The Wave Normal Angle and Ellipticity

Figures 7 and 8 present 2D maps for ellipticity and wave normal angle before anything is masked out. We also provide the results in a wider frequency range.

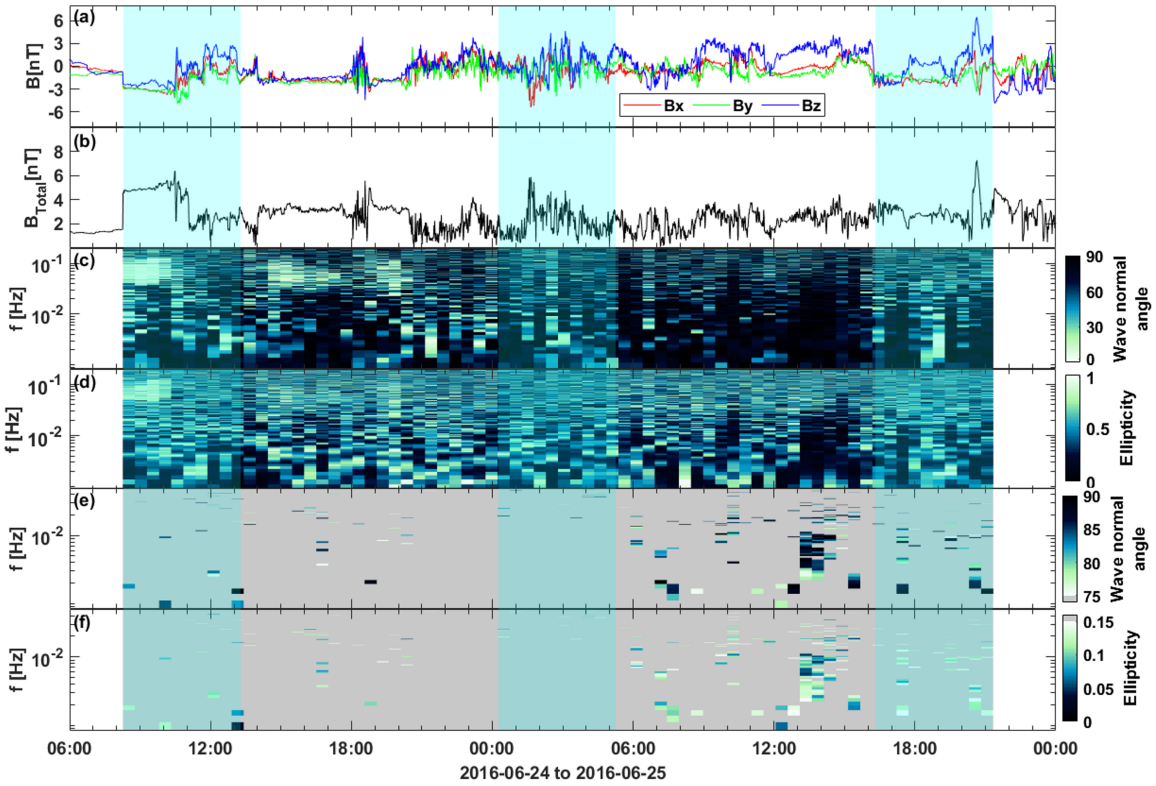

Figure 7. An example of the Jovian magnetosheath crossing event observed on the dawn flank. (a) The components of the magnetic field. (b) Total magnetic field. (c) Wave normal angle and (d) absolute value of ellipticity. (e) Wave normal angle and (f) absolute value of ellipticity with mask.

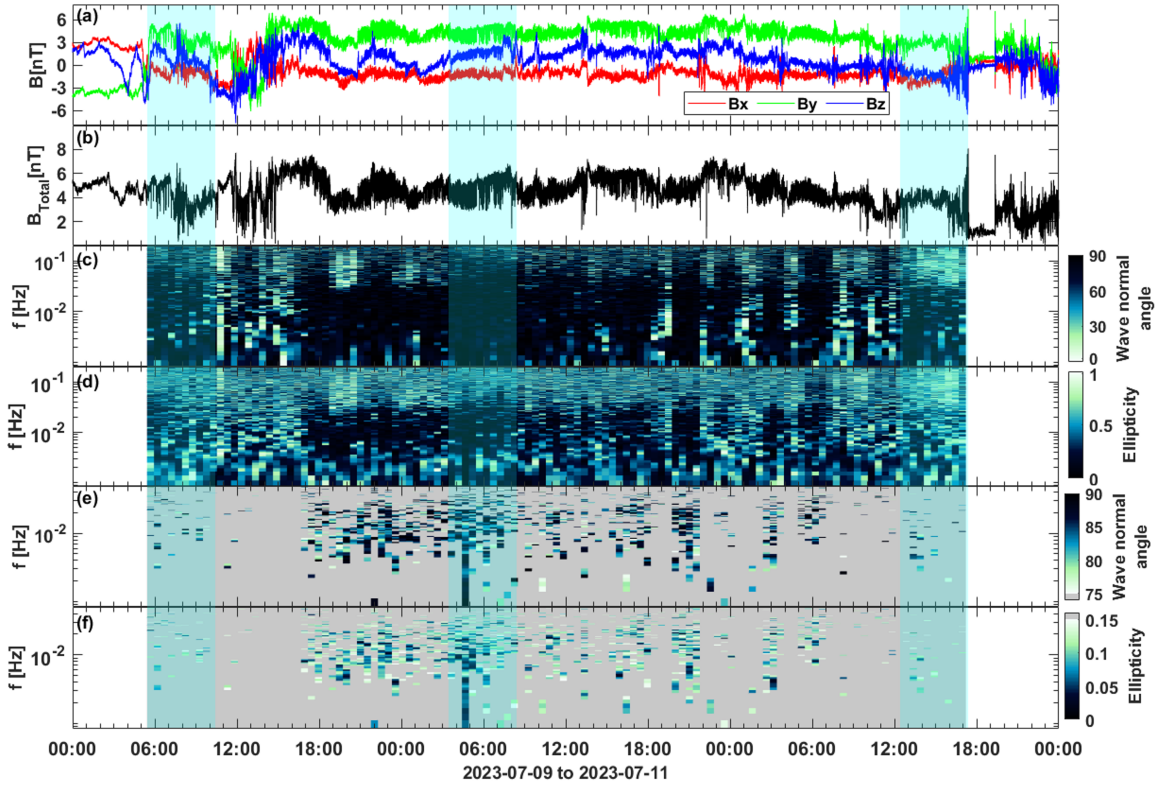

Figure 8. Similar plots to Figure 7 on the dusk flank.

Appendix B
The Magnetic Field Waveforms and Hodograms

We employed the MVA technique on the bandpass-filtered magnetic field fluctuations. Here, we selected the 2.5 hr intervals from each shaded region for analysis, with a filtering frequency band of 0.002–0.015 Hz.

Figure 9 presents the magnetic field waveforms on the dusk flank (Figure 3). Panel (a) shows the magnetic field waveforms in the middle MSH. Panel (b) shows the hodograms of the magnetic field fluctuations on their maximum and intermediate variance planes computed from the MVA technique. Panels (c)–(d) and (e)–(f) are similar plots in the BS vicinity and the MP vicinity. In the middle MSH, the magnetic fluctuations are mainly along the direction of maximum variance, showing the correlation between $\delta B_{\lambda\max}$ and $\delta B_{\lambda\mathrm{med}}$ components. S. W. Cyril et al. (2023) classified fluctuations with the ratio between maximum and intermediate eigenvalues $\lambda_{\max}/\lambda_{\mathrm{med}} \geqslant 2.5$, and intermediate and minimum eigenvalues $\lambda_{\mathrm{med}}/\lambda_{\min} \leqslant 8$ as nearly linearly polarized waves. The values of $\lambda_{\max}/\lambda_{\mathrm{med}}$ and $\lambda_{\mathrm{med}}/\lambda_{\min}$ are 12.25 and 2.00 in the middle MSH, 2.63 and 3.67 in the BS vicinity, and 1.40 and 3.68 in the MP vicinity, which also indicates the presence of waves exhibiting near-linear polarization in the middle MSH.

Figure 10 presents similar plots on the dawn flank (Figure 2). The values of $\lambda_{\max}/\lambda_{\mathrm{med}}$ and $\lambda_{\mathrm{med}}/\lambda_{\min}$ are 1.18 and 1.85 in the middle MSH, 1.72 and 1.19 in the BS vicinity, and 2.18 and 1.35 in the MP vicinity. We did not observe a significant correlation between $\delta B_{\lambda\max}$ and $\delta B_{\lambda\mathrm{med}}$ components.

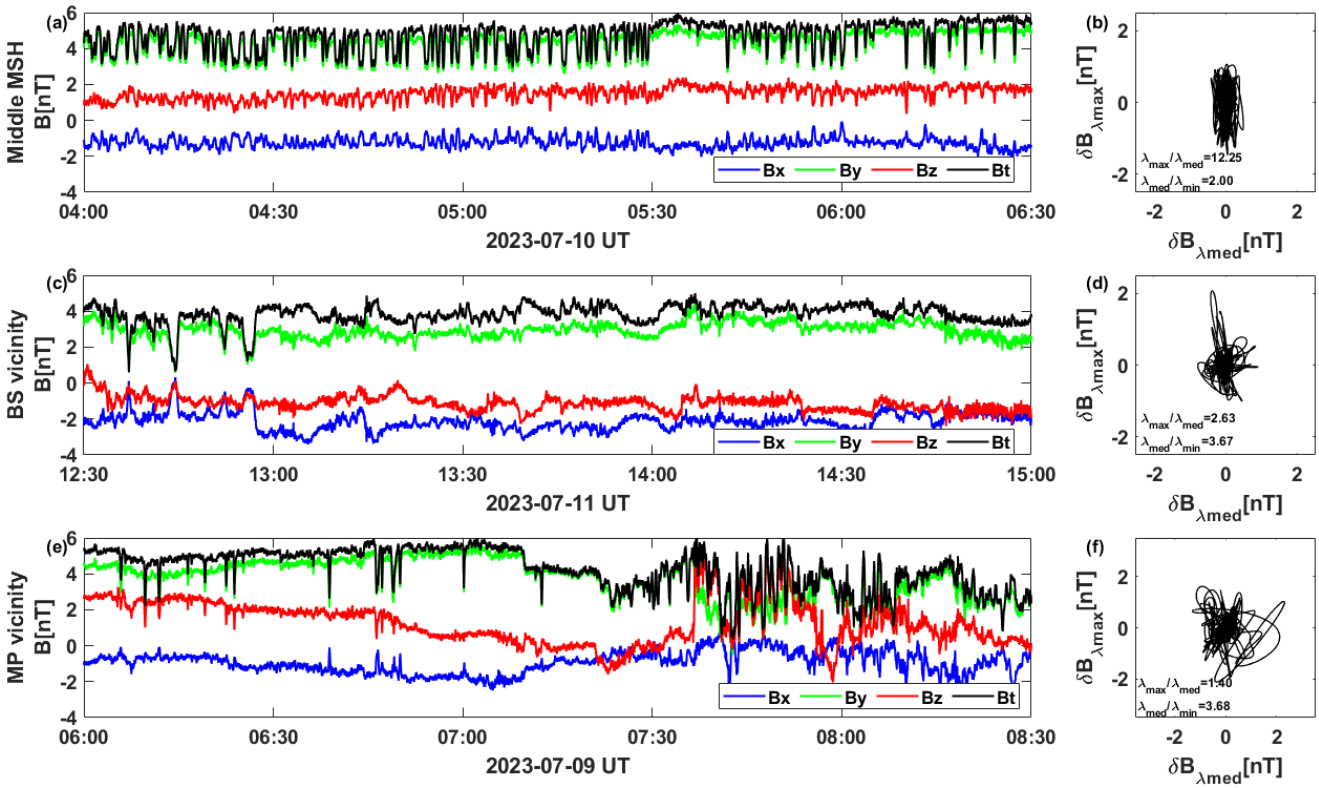

Figure 9. Magnetic field waveforms on the dusk flank. (a) The magnetic field waveforms. (b) The hodograms of the magnetic field fluctuations on their maximum and intermediate variance planes computed from the MVA technique. (c)–(d) and (e)–(f) plots similar to (a)–(b).

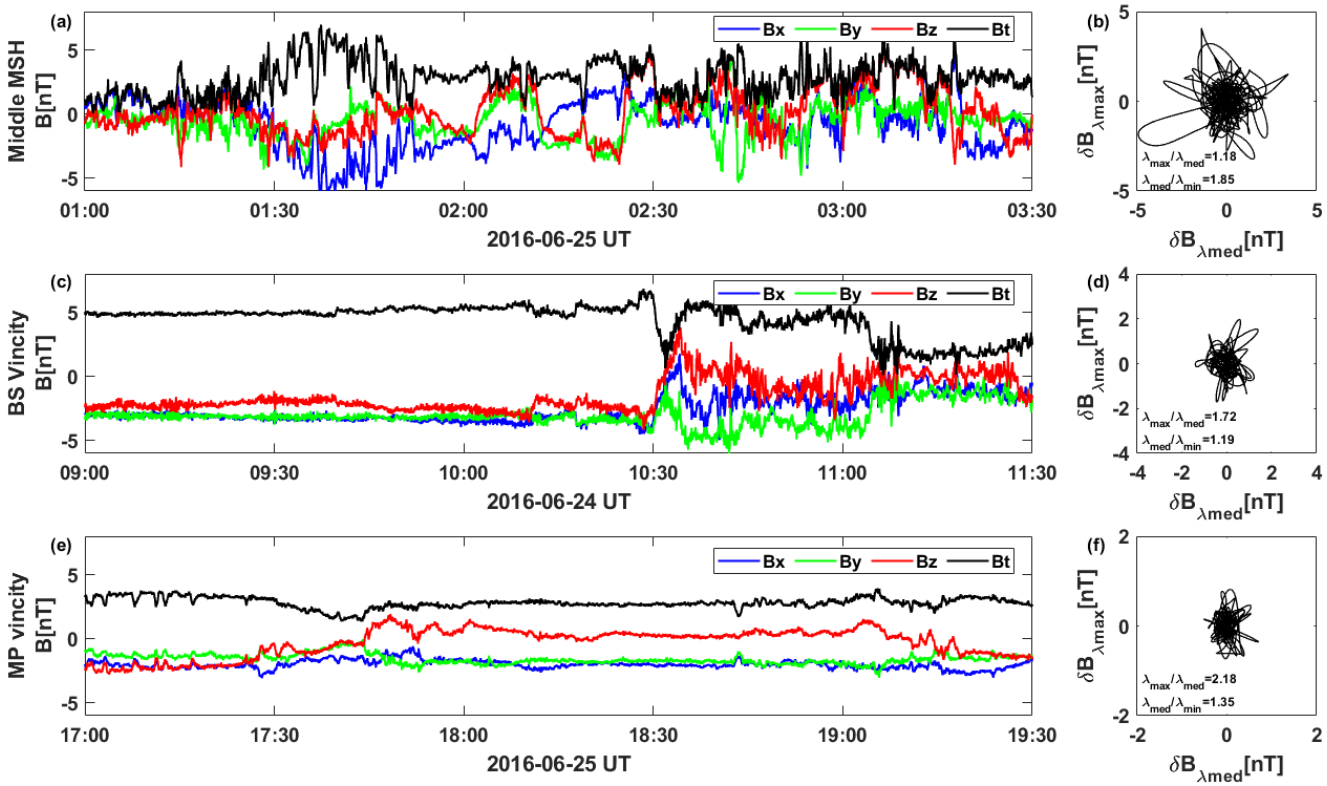

Figure 10. Similar plots to Figure 9 on the dawn flank.

ORCID iDs

Hui Li https://orcid.org/0000-0002-4839-4614
Zhongwei Yang https://orcid.org/0000-0002-1509-1529
Chi Wang https://orcid.org/0000-0001-6991-9398

References

Alexandrova, O., Lacombe, C., & Mangeney, A. 2008, AnGeo, 26, 3585
Anderson, R. R. 1983, RvGeo, 21, 474
Andrés, N., Bandyopadhyay, R., McComas, D. J., et al. 2023, ApJ, 945, 8
Bale, S. D., Kellogg, P. J., Mozer, F. S., Horbury, T. S., & Reme, H. 2005, PhRvL, 94, 215002
Bandyopadhyay, R., Chasapis, A., Chhiber, R., et al. 2018, ApJ, 866, 81
Bandyopadhyay, R., McComas, D. J., Szalay, J. R., et al. 2021, GeoRL, 48, e95006
Bolton, S. J., Lunine, J., Stevenson, D., et al. 2017, SSRv, 213, 5
Bolzan, M. J. A., & Echer, E. 2014, P&SS, 91, 77
Chen, C. H. K., Bale, S. D., Bonnell, J. W., et al. 2020, ApJS, 246, 53
Chhiber, R., Chasapis, A., Bandyopadhyay, R., et al. 2018, JGRA, 123, 9941
Connerney, J.E.P. 2024, NASA Planetary Data System
Connerney, J. E. P., Adriani, A., Allegrini, F., et al. 2017a, Sci, 356, 826
Connerney, J. E. P., Benn, M., Bjarno, J. B., et al. 2017b, SSRv, 213, 39
Cyril, S. W., Volwerk, M., Mazelle, C., et al. 2023, AnGeo, 41, 225
Dimmock, A. P., Yordanova, E., Graham, D. B., et al. 2022, JGRA, 127, e2022JA030754
Erdős, G., & Balogh, A. 1996, JGR, 101, A1
Hadid, L. Z., Sahraoui, F., Kiyani, K. H., et al. 2015, ApJL, 813, L29
Hasegawa, H., Fujimoto, M., Phan, T.-D., et al. 2004, Natur, 430, 755
Hospodarsky, G. B., Kurth, W. S., Bolton, S. J., et al. 2017, GeoRL, 44, 4506
Huang, S. Y., Hadid, L. Z., Sahraoui, F., Yuan, Z. G., & Deng, X. H. 2017, ApJL, 836, L10
Huang, S. Y., Wang, Q. Y., Sahraoui, F., et al. 2020, ApJ, 891, 159
Iroshnikov, P. S. 1964, SvA, 7, 566
Jiang, W., Li, H., Liu, X., Verscharen, D., & Wang, C. 2023, JGRA, 128, e2022JA030874
Joy, S. P., Kivelson, M. G., Walker, R. J., et al. 2006, JGRA, 111, A12212
Kennel, C. F., Edmiston, J. P., & Hada, T. 1985, Collisionless Shocks in the Heliosphere: A Tutorial Review, 34 (Washington, DC: American Geophysical Union), 1
Khotyaintsev, Y., Nilsson, T., Johansson, E. P. G., et al. 2024, IRFU-Matlab, v1.17.0, Zenodo, doi:10.5281/zenodo.14525047
Kolmogorov, A. 1941, DoSSR, 30, 301
Kraichnan, R. H. 1965, PhFl, 8, 1385
Kunz, M. W., Schekochihin, A. A., & Stone, J. M. 2014, PhRvL, 112, 205003
Kurth, W. S., & Piker, C. W. 2024, NASA Planetary Data System
Kurth, W. S., Hospodarsky, G. B., Kirchner, D. L., et al. 2017, SSRv, 213, 347
Li, H., Jiang, W., Wang, C., et al. 2020, ApJL, 898, L43
Li, H., Jiang, W., Yang, Z., et al. 2024, ApJ, 967, 76
Lucek, E. A., Dunlop, M. W., Balogh, A., et al. 1999, AnGeo, 17, 1560
Macek, W. M., Krasińska, A., Silveira, M. V. D., et al. 2018, ApJL, 864, L29
Matsumoto, Y., & Hoshino, M. 2004, GeoRL, 31, L02807
McComas, D. J., Szalay, J. R., Allegrini, F., et al. 2017, GeoRL, 44, 4432
Ranquist, D. A., Bagenal, F., Wilson, R. J., et al. 2019, JGRA, 124, 9106
Roberts, O. W., Narita, Y., Nakamura, R., & Vörös, Z. 2023, A&A, 677, L16
Sahraoui, F., Belmont, G., Rezeau, L., et al. 2006, PhRvL, 96, 075002
Sahraoui, F., Goldstein, M. L., Robert, P., & Khotyaintsev, Y. V. 2009, PhRvL, 102, 231102
Santolík, O., Parrot, M., & Lefeuvre, F. 2003, RaSc, 38, 1010
Scarf, F. L., Gurnett, D. A., Kurth, W. S., & Poynter, R. L. 1979, Natur, 280, 796
Shoji, M., Omura, Y., Tsurutani, B. T., Verkhoglyadova, O. P., & Lembege, B. 2009, JGRA, 114, A10203
Soucek, J., Escoubet, C. P., & Grison, B. 2015, JGRA, 120, 2838
Stawarz, J. E., Eastwood, J. P., Phan, T. D., et al. 2022, PhPl, 29, 012302
Stawarz, J. E., Eriksson, S., Wilder, F. D., et al. 2016, JGRA, 121, 11021
Tsurutani, B. T., Lakhina, G. S., Verkhoglyadova, O. P., et al. 2011, JGRA, 116, A02103
Volwerk, M., Schmid, D., Tsurutani, B. T., et al. 2016, AnGeo, 34, 1099
Volwerk, M., Zhang, T. L., Delva, M., et al. 2008, GeoRL, 35, L12204
Wu, P., Winske, D., Gary, S. P., Schwadron, N. A., & Lee, M. A. 2009, JGRA, 114, A08103
Xiao, S., Zhang, T. L., Vörös, Z., et al. 2020, JGRA, 125, e2019JA027190
Zhao, L.-L., Zank, G. P., Opher, M., et al. 2024, ApJ, 973, 26
Zimbardo, G., Greco, A., Sorriso-Valvo, L., et al. 2010, SSRv, 156, 89